Chapter

Flux Reversal Machine Design

Yuting Gao and Yang Liu

Abstract

Flux reversal permanent magnet machines (FRPMMs) have a simple reluctance rotor and a stator with armature windings and permanent magnets (PMs). Due to the high torque density and high efficiency of FRPMMs, they have been widely used in many applications such as electric vehicle, wind power generation, etc. However, the general design method of FRPMMs has not been established in books. Therefore, this chapter will focus on introducing an analytical design method, which allows for fast design of FRPMMs. First of all, the analytical sizing equations are deduced based on a magneto motive force (MMF)-permeance model. After that, the effects of some key performances including average torque, pulsating torque, power factor, and PM demagnetization are analyzed. Moreover, the feasible slot-pole combinations are summarized and the corresponding winding type of each combination is recommended in order to maximize the output torque. Besides, the detailed geometric design of stator and rotor are presented. Finally, a case study is presented to help readers better understand the introduced design methodology.

Keywords: design method, flux reversal permanent magnet machine (FRPMM), sizing equation, finite element analysis (FEA)

1. Introduction

The topology of FRPMM is depicted in **Figure 1**. As can be seen, it has a slotted rotor without any windings or PMs, and a stator with armature windings and PMs mounted on each stator teeth. First of all, the structural characteristics of FRPMMs and the corresponding performance advantages need to be explained:

1. FRPMMs are excited by PMs instead of the excitation windings, which are different with asynchronous motors and brushed DC motors. So, for FRPMMs, the rotor will not have copper losses, and the efficiency is relatively higher [1, 2].

2. The rotor of FRPMMs has no windings or permanent magnets, thus is suitable for high-speed operation and high-temperature operating conditions [3]. Moreover, the no excitation winding will keep away from the problems of friction noise and electric spark. So, FRPMMs are more reliable and require less maintenance [4, 5]. In addition, the rotor of FRPMMs is light in weight and has a small rotational inertia [6]; hence, the acceleration and deceleration response is faster.

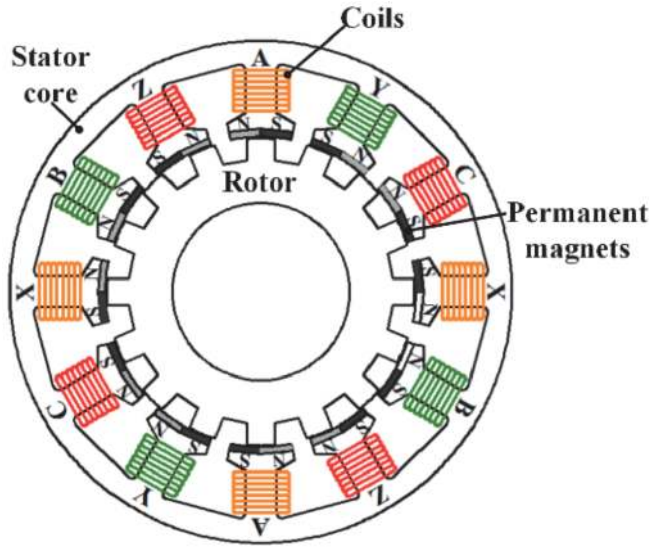

Figure 1.
Cross section of a FRPMM.

3. The stator windings of FRPMMs are mostly concentrated windings, which are easy to manufacture. Moreover, the electromagnetic isolation of the concentrated windings is better than regular distributed windings, which means that if one winding has faults, the fault is not likely to spread to other windings, and thus the fault tolerance is good [7, 8]. In addition, the concentrated winding has a smaller winding factor, inductance, and a shorter electrical time constant than the distributed windings [9], and thus the dynamic response of concentrated winding is faster.

4. Compared to other stator-PM machines, that is, flux switching PM machines and doubly salient PM machines, FRPMMs have a simpler structure. The PMs of the flux switching PM machines and doubly salient PM machines are inserted into the stator core, which is not convenient for installation. In the flux switching PM machine, putting permanent magnets in the middle of the teeth will reduce the slot area and affect the output torque. In the doubly salient PM machine, placing PMs in the yoke will increase the volume of the motor and reduce the torque density. In the FRPMMs, the PMs are pasted on the inner surface of the stator teeth, thus eliminating the above problems [10].

Finally, the structural characteristics and performance advantages of the flux-reverse motor can be summarized in **Table 1**.

It can be seen that the FRPMMs have many performance advantages, and these advantages can be utilized in different applications. First of all, the high efficiency, the large torque density, the rapid acceleration, and deceleration response make FRPMMs suitable for various high-speed rotation areas, such as electric vehicles [11–13], electric spindle [14], fans [15, 16], etc. Secondly, the number of rotor pole pairs is usually high, which is also suitable for low-speed areas, meanwhile its torque density is high at the low speeds, making FRPMMs suitable for various low-speed direct-drive occasions [17], for example wind power [18–20], direct drive servo system [21], wave power generation [22], etc. In addition, linear FRPMM has no PMs and copper windings in the secondary, which saves cost and is also very suitable for long rail transit linear motion applications [23, 24].

No.	Structural characteristic	Advantages
1	Use rare-earth PMs	1. No excitation loss, high motor efficiency; 2. Rare-earth with high-magnetic energy product increases torque density
2	No windings or PMs in the rotor	1. Simple rotor structure, suitable for high-speed operation and high temperature conditions; 2. Avoids mechanical friction and electric sparks caused by commutators and brushes, thus improving the reliability; 3. Small rotational inertia, thus fast acceleration and deceleration response
3	Often use concentrated windings	1. Good fault tolerance and high reliability; 2. Easy processing and manufacturing; 3. Small inductance and electrical time constant
4	PMs attached to the stator teeth surface	1. Easy to install 2. No reduction in the slot area or increase in the motor volume

Table 1.
Structural characteristics and corresponding advantages of FRPMM.

In most existing literatures, the design of FRPMMs is mainly based on the classical design method [25] with low accuracy or time-consuming finite element algorithm (FEA) [26]. Therefore, in this chapter, the specialized sizing equations for FRPMMs will be deduced and the analytical design method will be introduced, which can be directly employed in the initial design of FRPMMs and allows for fast calculations of machine dimensions.

This chapter is organized as follows. First, the structure and operation principles are introduced in Section 2. Then in Section 3, the magnetic circuit model is built and the sizing equations are analytically derived. After that, in Section 4, the influences of several key parameters (slot-pole combination, airgap radius, electric loading, and equivalent magnetic loading) in the sizing equation on the torque density are analyzed. Also, the effects of the airgap structural parameters on the pulsating torque, power factor, and PM demagnetization performances are investigated. Moreover, in Section 5, the geometric design of stator and rotor are introduced. And in Section 6, the design procedure is illustrated. Besides, to make the analytical design method more readable, a case study is presented and a FRPMM prototype is tested. Finally, conclusions are drawn in Section 7.

2. Operation principle of FRPMM

To clearly exhibit the operating principle, a three-phase FRPMM with two pole windings, six stator slots, and eight rotor teeth is cited as an example. The flux distributions at different rotor positions are illustrated in **Figure 2**. The magnetic flux field is excited only by the PMs, and the difference of each rotor movement is 11.25 mech. degrees (i.e., 1/4 rotor slot pitch). Taking flux linkage of phase A winding as an example, when the rotor position is 0 degree, the flux linkage is 0; when the rotor position is 11.25 mech. degree (90 elec. degree), the flux linkage reaches the positive maximum value; when the rotor position is 22.5 mech. degree (180 elec. degree), the flux linkage is 0; when the rotor position is 33.75 mech. degree (270 elec. degree), the flux linkage reaches the negative maximum value. Therefore, in the duration of one rotor slot pitch (360 elec. degrees), the winding flux linkage reverses the polarity, thus it is called "flux reversal machine." Then,

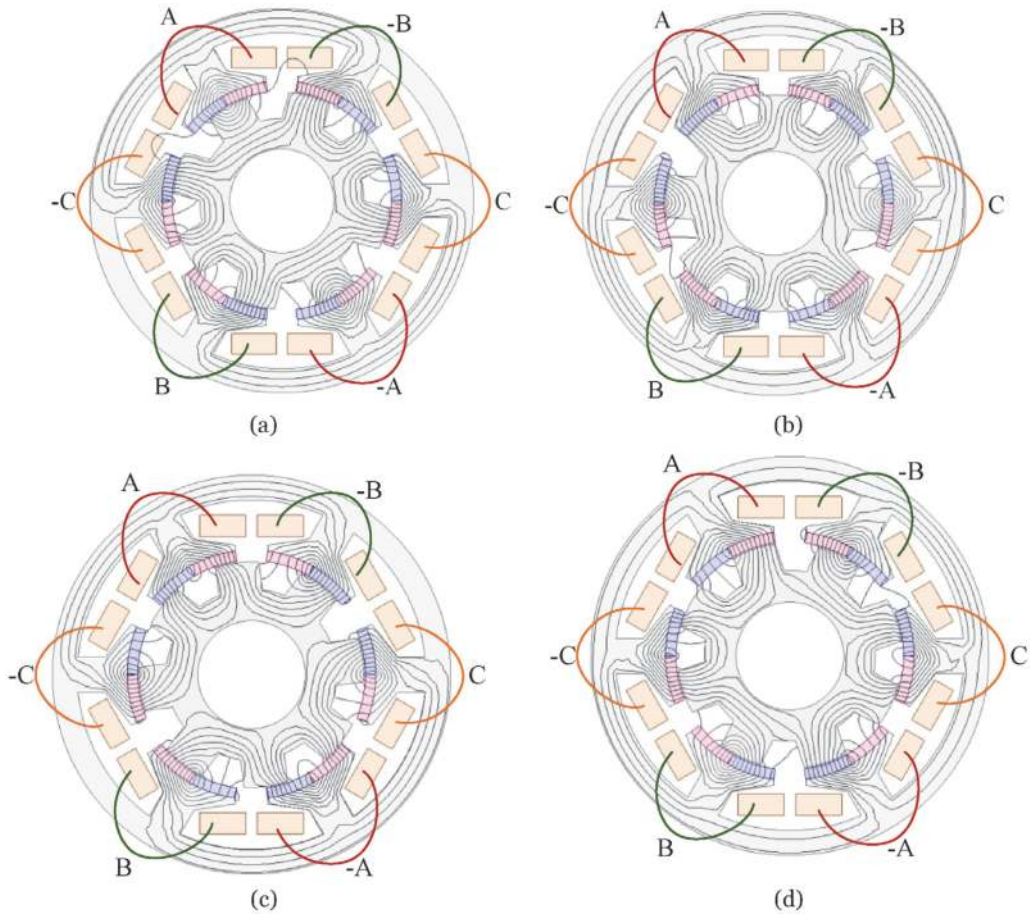

Figure 2.
No-load flux lines of the FRPMM excited by the PMs: (a) rotor position =0 elec. degree; (b) rotor position =90 elec. degree; (c) rotor position =180 elec. degree; (d) rotor position =270 elec. degree.

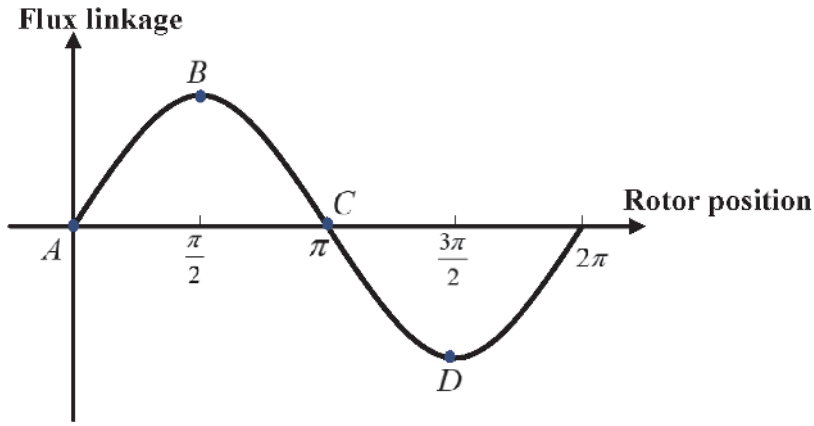

Figure 3.
Variation of flux linkage of phase a winding at different rotor positions.

after obtaining the bipolar flux linkage, as shown in **Figure 3**, the winding can produce a bipolar back-electromagnetic motive force (EMF). If the armature windings are injected with currents having the same frequency and phase with the back-EMF, a steady torque can be yielded.

3. Sizing equation of FRPMM

3.1 Magnetic circuit model

In order to derive the sizing equation of FRPMMs, the magnetic circuit model should be built at first; then, based on the model, the analytical equations of airgap flux density, back-EMF, and torque will be deduced.

The equivalent magnetic circuit model can be plotted as **Figure 4**. At No.1 stator tooth, its magnetic field distribution corresponds to the position shown in **Figure 2(b)**, that is, the rotor tooth is closer to the S-pole magnet. The S-pole magnetic generates two paths of magnetic flux, one is pole leakage flux Φ_{pl}, which goes through the adjacent N-pole magnet, the other is main flux Φ_m, which goes through the stator tooth, stator yoke, rotor tooth, and rotor yoke, thus can provide winding flux linkage and back-EMF. At No. 2 stator tooth, its magnetic field distribution corresponds to the position shown in **Figure 2(c)**, that is, the rotor axis is at the same distance from the S-pole and N-pole magnets. Thus, at this time, the two magnets can only generate one magnetic flux path, that is, the pole leakage flux Φ_{pl}. At No. 3 stator tooth, its magnetic field distribution corresponds to the position shown in **Figure 2(d)**, that is, the rotor tooth is closer to the N-pole magnet. The N-pole magnetic generates two paths of magnetic flux, one is pole leakage flux Φ_{pl}, which goes through the adjacent S-pole magnet, the other is main flux Φ_m, which goes through the stator tooth, stator yoke, rotor tooth, and rotor yoke, thus can provide winding flux linkage and back-EMF. It should be noted that the magnetic flux path of No. 1 stator tooth is just opposite to that of No. 3 stator tooth, so winding flux polarity in these two cases is just opposite to each other.

As mentioned above, **Figure 4** provides the magnetic circuit of FRPMMs, which can help analyze the flux distribution of FRPMMs at different rotor positions. However, the magnetic circuit requires the establishment of the whole FRPMM

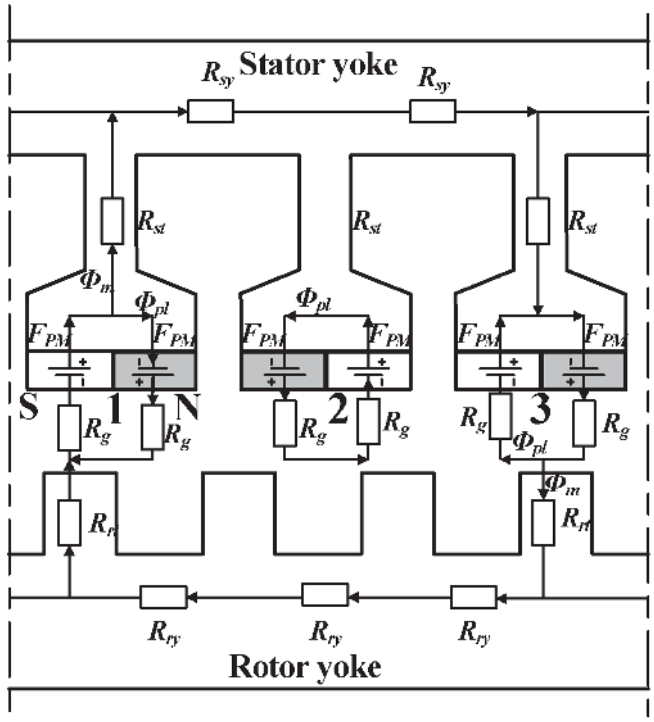

Figure 4.
Equivalent magnetic model of FRPMMs.

magnetic path, which is rather complex. Besides, the pole leakage flux, main flux, and the reluctance at each rotor positions should be calculated, which needs high workload. Therefore, a simplified magnetic circuit should be built. Observing **Figure 2**, it can be seen that a small rotor displacement brings a large rotation in stator flux field. This phenomenon is called as flux modulation effect, i.e. a high-pole slow-speed magnetic field becomes a low-pole high-speed magnetic field through the modulation effect of iron teeth. Therefore, the physical nature of FRPMM is indeed the flux modulation effect. The research of some flux modulation machines are usually based on the PM magnetic motive force (MMF)-airgap permeance model, such as the Vernier machine in [27]. So, this chapter will use this model to analyze FRPMMs.

In PM MMF-airgap permeance model, the no-load airgap flux density $B(\theta_s,\theta)$ can be written as the product of PM MMF $F_{PM}(\theta_s)$ and specific airgap permeance $\Lambda(\theta_s,\theta)$:

$$B(\theta_s,\theta) = F_{PM}(\theta_s)\Lambda(\theta_s,\theta) \tag{1}$$

where the definitions of angles θ_s and θ are shown in **Figure 5**. Then, the simplified magnetic circuit model can be given in **Figure 6**. Once knowing the PM

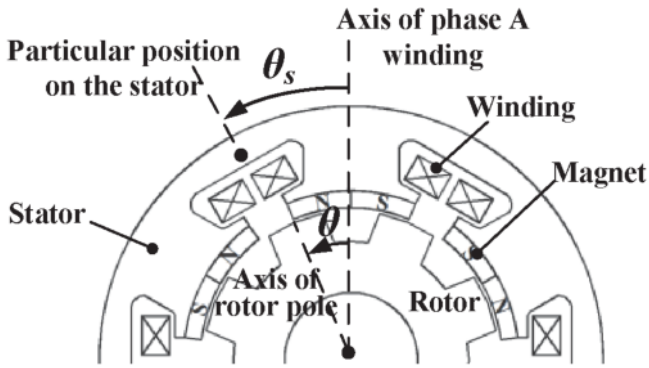

Figure 5.
Definitions of different angles in FRPMM.

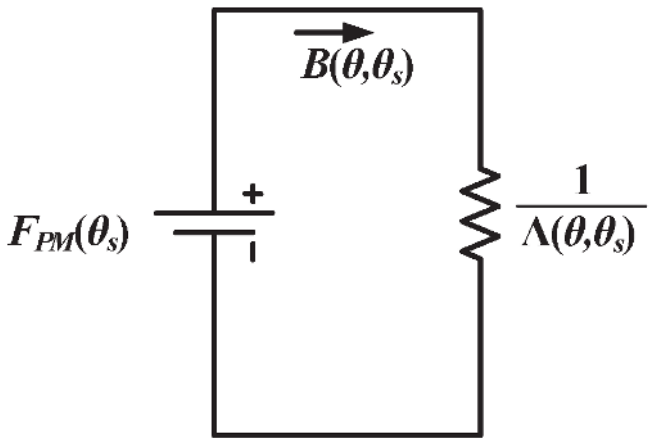

Figure 6.
Simplified equivalent magnetic model of FRPMMs.

MMF and airgap permeance, the no-load airgap flux density can be obtained. Then, the stator flux linkage $\lambda_{ph}(\theta)$ can be deduced using winding function theory:

$$\lambda_{ph}(\theta) = r_g l_{stk} \int_0^{2\pi} B(\theta_s, \theta) N(\theta_s) d\theta_s \tag{2}$$

where $N(\theta_s)$ is the phase winding function. After that, the phase back-EMF $E_{ph}(t)$ and average torque T_e can be calculated as:

$$E_{ph}(t) = \frac{d\lambda_{ph}(\theta)}{dt} \tag{3}$$

$$T_e = \frac{3}{2} E_{ph} I_{ph} \tag{4}$$

where I_{ph} is the peak value of phase current. Therefore, from Eqs. (1–4), it can be found that if the torque equation need to be calculated, the key is to obtain the equation of airgap flux density $B(\theta_s,\theta)$, which is further determined by the PM MMF $F_{PM}(\theta_s)$ and specific airgap permeance $\Lambda(\theta_s,\theta)$. Therefore, in the next parts, the equations of the PM MMF $F_{PM}(\theta_s)$ and specific airgap permeance $\Lambda(\theta_s,\theta)$ will be deduced in detail.

3.2 Airgap flux density equation

As aforementioned, to derive the torque equation, the no-load airgap flux density $B(\theta_s,\theta)$ should firstly be known, whose equation can be given as Eq. (1). Then, the next step is to derive the expressions of $F_{PM}(\theta_s)$ and $\Lambda(\theta_s,\theta)$. The PM MMF waveform excited by the magnets is shown in **Figure 7**, which can be given as:

$$F_{PM}(\theta_s) = \begin{cases} F_C; & 0 \le \theta_s < (1-SO)\pi/Z_s \\ 0; & (1-SO)\pi/Z_s \le \theta_s < (1+SO)\pi/Z_s \\ F_C; & (1+SO)\pi/Z_s \le \theta_s < 2\pi/Z_s \\ -F_C; & 2\pi/Z_s \le \theta_s < (3-SO)\pi/Z_s \\ 0; & (3-SO)\pi/Z_s \le \theta_s < (3+SO)\pi/Z_s \\ -F_C; & (3+SO)\pi/Z_s \le \theta_s < 4\pi/Z_s \end{cases} \tag{5}$$

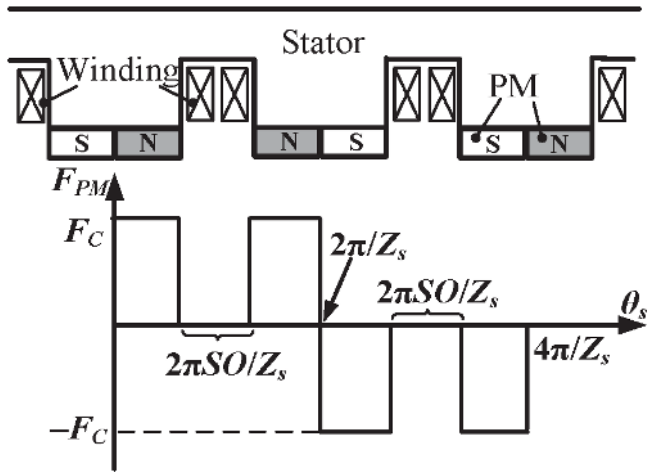

Figure 7.
Magnet MMF waveform.

where F_C is:

$$F_C = \frac{B_r h_m}{\mu_r \mu_0} \tag{6}$$

Then, it can be written in Fourier series as follows:

$$F_{PM}(\theta_s) = \sum_{i=1,3,5}^{\infty} F_i \sin\left(\frac{iZ_s}{2}\theta_s\right) \tag{7}$$

where the magnitude F_i is

$$F_i = \frac{4}{\pi}\frac{1}{i}\frac{B_r h_m}{\mu_0 \mu_r}\left[1 + (-1)^{\frac{i+1}{2}} \sin\left(\frac{i\pi}{2} SO\right)\right] \tag{8}$$

Then, the next step is to derive the specific airgap permeance $\Lambda(\theta_s,\theta)$ in Eq. (1). Since the stator slotting effect has already been considered in Eqs. (5–8), the specific airgap permeance $\Lambda(\theta_s,\theta)$ can be replaced by the airgap permeance with smoothed stator and slotted rotor $\Lambda_r(\theta_s,\theta)$. The model of smoothed stator and slotted rotor is shown in **Figure 8**. Then, the $\Lambda_r(\theta_s,\theta)$ can be expressed by:

$$\Lambda_r(\theta_s, \theta) \approx \Lambda_{0r} + \Lambda_{1r} \cos\left[Z_r(\theta_s - \theta)\right] \tag{9}$$

The coefficients of the airgap permeance function Λ_{0r} and Λ_{1r} in Eq. (9) can be obtained using the conformal mapping method [28, 29]:

$$\Lambda_{0r} = \frac{\mu_0}{g'}\left(1 - 1.6\beta\frac{b_o}{t}\right) \tag{10}$$

$$g' = g + h_m/\mu_r \tag{11}$$

$$\Lambda_{1r} = \frac{\mu_0}{g'}\frac{4}{\pi}\beta\left[0.5 + \frac{(b_o/t)^2}{0.78125 - 2(b_o/t)^2}\right]\sin\left(1.6\pi\frac{b_o}{t}\right) \tag{12}$$

$$\beta = 0.5 - \frac{1}{2\sqrt{1 + \left(\frac{b_o}{2t}\frac{t}{g'}\right)^2}} \tag{13}$$

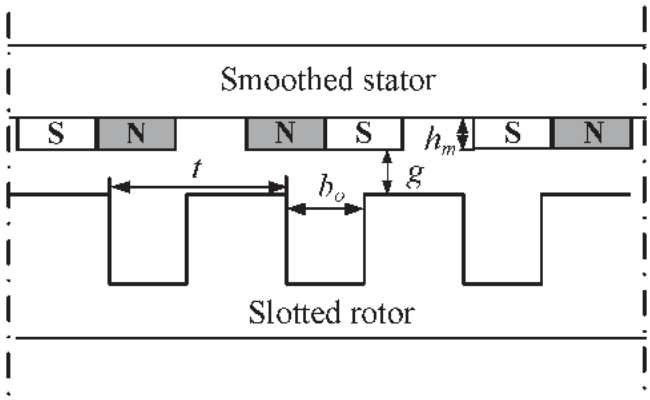

Figure 8.
Schematic of single-side salient structure on rotor.

where b_o is the rotor slot opening width and t is the rotor slot pitch, as shown in **Figure 8**. Combining Eq. (1), Eqs. (5–13), the no-load airgap flux density $B(\theta_s,\theta)$ can be finally calculated as:

$$B(\theta_s,\theta)=\sum_{i=1,3}^{\infty}B_i\sin\left[\left(\frac{iZ_s}{2}\pm Z_r\right)\theta_s-Z_r\theta\right] \tag{14}$$

where the magnitude B_i is

$$B_i=\frac{1}{2}F_i\Lambda_{1r},\ i=1,3,5\ldots \tag{15}$$

3.3 Slot-pole combinations

As can be seen in Eq. (14), the number of pole pairs in the air gap flux density is $iZ_s/2\pm Z_r$, i = 1,3,5 … Then, in order to make the flux density induce EMF in the armature windings, the pole pair number of the armature windings P should be equal to $iZ_s/2\pm Z_r$, i = 1,3,5 … Besides, for three phase symmetry, the winding pole pair number must also meet the following requirement:

$$\frac{Z_s}{GCD(Z_s,P)}=3k,\ k=1,2,3\ldots \tag{16}$$

All in all, the slot-pole combination of three-phase FRPMMs is ruled by the following equation:

$$\begin{aligned}&P=\min\left\{P=\frac{iZ_s}{2}\pm Z_r;\quad\frac{Z_s}{GCD(Z_s,P)}=3k\right\}\\&i=1,3,5\ldots\quad k=1,2,3\ldots\end{aligned} \tag{17}$$

where min means to select the minimum number of these qualified harmonic orders so as to obtain a maximal pole ratio of FRPMMs. Therefore, the feasible slot-pole combinations can be summarized as **Table 2**. Non-overlapping windings (i.e., concentrated windings) are usually used in FRPMMs because of the higher fault tolerance and easier manufacture than regular overlapping windings. However, some FRPMMs are suggested to employ overlapping windings in order to have a larger winding factor and thus a higher torque density. Therefore, both winding factors, that is, k_{wn} (using non-overlapping winding) and k_{wr} (using overlapping winding) are calculated for each FRPMM so as to see the difference of using different winding types.

3.4 Torque equation

Once the stator winding pole pair is selected, the stator flux linkage can be deduced using winding function theory, just as mentioned in Eq. (2). The winding function $N(\theta_s)$ in Eq. (2) can be written as:

$$N(\theta_s)=\sum_{i=1,3,5}^{\infty}N_i\cos\left(iP\theta_s\right) \tag{18}$$

$$N_i=\frac{2}{i\pi}\frac{N_s}{P}k_{wi} \tag{19}$$

Z_s	Z_r	2	3	4	5	6	7	8	10	11	12	13	14	15	16
6	*P*	1		1	2		2	1	1	2		2	1		1
	SPP	1		1	0.5		0.5	1	1	0.5		0.5	1		1
	PR	2		4	2.5		3.5	8	10	5.5		6.5	14		16
	k_{wn}	0.5		0.5	0.866		0.866	0.5	0.5	0.866		0.866	0.5		0.5
	k_{wr}	1		1	0.866		0.866	1	1	0.866		0.866	1		1
12	*P*	4		2	1		1	2	4	5		5	4		2
	SPP	0.5		1	2		2	1	0.5	0.4		0.4	0.5		1
	PR	0.5		2	5		7	4	2.5	2.2		2.6	3.5		8
	k_{wn}	0.866		0.5	0.25		0.25	0.5	0.866	0.933		0.933	0.866		0.5
	k_{wr}	0.866		1	0.966		0.966	1	0.866	0.933		0.933	0.866		1
18	*P*	7	6	5	4	3	2	1	1	2	3	4	5	6	7
	SPP	3/7	0.5	0.6	0.75	1	1.5	3	3	1.5	1	0.75	0.6	0.5	3/7
	PR	2/7	0.5	0.8	1.25	2	3.5	8	10	5.5	4	3.25	2.8	2.5	16/7
	k_{wn}	0.902	0.866	0.735	0.617	0.5	0.492	0.167	0.167	0.492	0.5	0.617	0.735	0.866	0.902
	k_{wr}	0.902	0.866	0.945	0.945	1	0.945	0.96	0.96	0.945	1	0.945	0.945	0.866	0.902
PS:	Non-overlapping winding is recommended.									Other: Overlapping winding is recommended.					

k_{wn} *and* k_{wr} *are fundamental winding factors calculated based on non-overlapping winding type and recommended winding types, respectively.*

Table 2.
Slot-pole combinations of three-phase FRPMM.

where N_i is the ith harmonics of the winding function and k_{wi} is the winding factor of the ith harmonics. As can be seen in Eq. (17), the pole pair number is $iZ_s/2 \pm Z_r$ (i = 1,3,5 ...). So, the sum or difference of any two pole pair harmonics P_{i1} and P_{i2} is a multiple of stator slot number, that is,

$$\begin{cases} P_{i1} = i_1 Z_s/2 \pm Z_r \\ P_{i2} = i_2 Z_s/2 \pm Z_r \\ |P_{i1} \pm P_{i2}| = kZ_s, \quad k = 1, 2, 3 \ldots \end{cases} \tag{20}$$

Therefore, all the flux density harmonics are tooth harmonics of each other, that is, they have the same absolute values of winding factors, and their absolute winding factor equals the fundamental winding factor k_{w1}:

$$|k_{wP_{i1}}| = |k_{wP_{i2}}| = k_{w1} \tag{21}$$

Then, combining Eq. (2), Eq. (3), Eqs. (18–21), the back-EMF can be finally obtained as:

$$E_{ph} = 2\omega_m r_g l_{stk} N_s Z_r k_{w1} \sum_{i=1}^{\infty} \text{sgn} * \frac{B_i}{\left(\frac{iZ_s}{2} \pm Z_r\right)/P} \tag{22}$$

where

$$\text{sgn} = \begin{cases} 1, \text{winding factor of } (iZ_s/2 \pm \mathrm{Z}_r)^{\text{th}} \text{ harmonic equals } k_{w1} \\ -1, \text{winding factor of } (iZ_s/2 \pm \mathrm{Z}_r)^{\text{th}} \text{ harmonic equals } -k_{w1} \end{cases} \tag{23}$$

Since the reluctance torque of FRPMM is negligible, the electromagnetic torque under i_d = 0 control can be expressed as Eq. (4). Then, combining Eq. (4) and Eq. (22), the average torque T_e is able to be calculated as:

$$T_e = 3I_{ph} r_g l_{stk} N_s Z_r k_{w1} \sum_{i=1}^{\infty} \text{sgn} * \frac{B_i}{\left(\frac{iZ_s}{2} \pm Z_r\right)/P} \tag{24}$$

So far, the general torque equation has been obtained as Eq. (24), but in this equation, some parameters such as B_i, I_{ph} cannot be determined in the initial design stage of FRPMMs, so it is desirable that Eq. (24) can be transformed to a combination of several basic parameters, such as electric loading, magnetic loading, which can be easily determined in the initial design stage.

As known for electrical machines, the electric loading A_e can be written as:

$$A_e = \frac{6N_s I_{ph}}{2\sqrt{2}\pi r_g} \tag{25}$$

Then, the equivalent magnetic loading of three-phase FRPMM B_m is defined as:

$$B_m = \sum_{i=1}^{\infty} \text{sgn} * \frac{B_i}{\left(\frac{iZ_s}{2} \pm Z_r\right)/P} \tag{26}$$

So, the torque expression in Eq. (24) can be rewritten as:

$$T_e = \sqrt{2}\pi r_g^2 l_{stk} k_w Z_r A_e B_m \tag{27}$$

Thus, the rotor volume V_r, which equals $\pi l_{stk} r^2 g$, can be obtained:

$$V_r = \frac{T_e}{\sqrt{2} k_w Z_r A_e B_m} \tag{28}$$

and then the airgap radius r_g and the stack length l_{stk} can be derived as:

$$r_g = \sqrt[3]{V_r/(\pi k_{lr})} \tag{29}$$

$$l_{stk} = \sqrt[3]{V_r k_{lr}^2/\pi} \tag{30}$$

where k_{lr} is the aspect ratio, equals to the ratio of r_g to l_{stk}. It can be found in Eq. (27) that the key parameters affecting the torque density are the airgap radius r_g, stack length l_{stk}, winding factor k_w, rotor slot number Z_r, electric loading $A_{e,}$ and equivalent magnetic loading B_m, among which the stack length l_{stk} can be determined by the volume requirement, and winding factor k_w is approximate to 1. So, the remaining parameters r_g, Z_r, A_e, B_m should be determined at the initial stage of the design process. Thus, the influences of the above key parameters on important performances, such as average torque, pulsating torque, power factor, PM demagnetization performance, will be investigated in the following parts.

4. Influence of design parameters on key performances

4.1 Average torque performances

4.1.1 Influence of slot-pole combinations on average torque

As aforementioned, the rotor slot number Z_r is one of key parameters that should be determined in the first design stage. How to determine the rotor slot number is a question. In this part, the influence of Z_r on the torque performance will be investigated, giving instruction on how to select Z_r. The parameters of the FRPMM models are listed in **Table 3**. These parameters are kept the same for the FRPMMs in order to have a reasonable comparison of their torque performance. That is to say, the airgap radius r_g, stack length l_{stk}, and electric loading A_e are the same.

Figure 9 shows the influence of rotor slot number on the output torque when non-overlapping windings and recommended windings are used respectively. For **Figure 9(a)**, when non-overlapping windings are adopted, the average torque is mainly related to the product of winding factor and rotor slot number, that is,

Parameter	Value	Parameter	Value
Stator outer diameter	170 mm	Stator inner diameter	105 m
Stator slot opening ratio	0.25	Remanent permeability	1.065
Stack length	100 mm	PM thickness	2.5 mm
Series turns per phase	80	Airgap length	0.5 mm
Rotor slot opening ratio	0.65	Rated current	5.3A
Rated speed	600 rpm	Magnet remanence	1.21 T

Table 3.
Parameters of the three-phase FRPMM models.

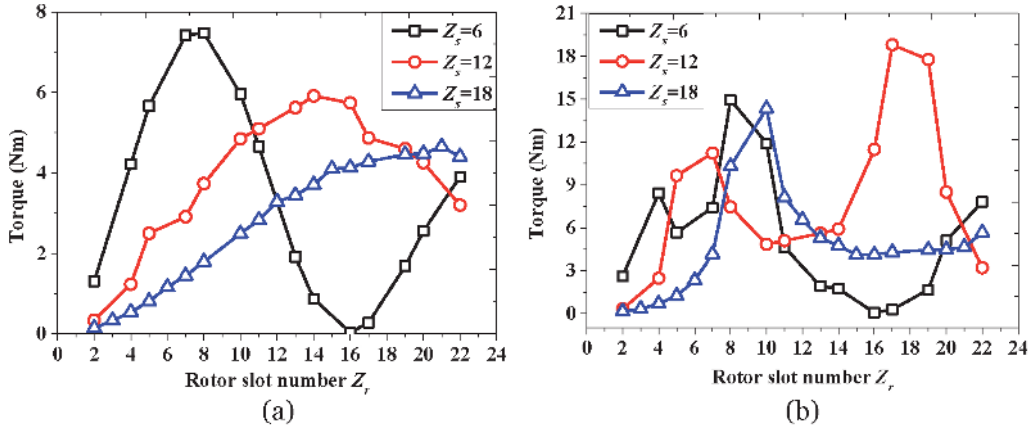

Figure 9.
Effect of combinations of stator slots and rotor slots on torque: (a) non-overlapping windings; (b) recommended windings.

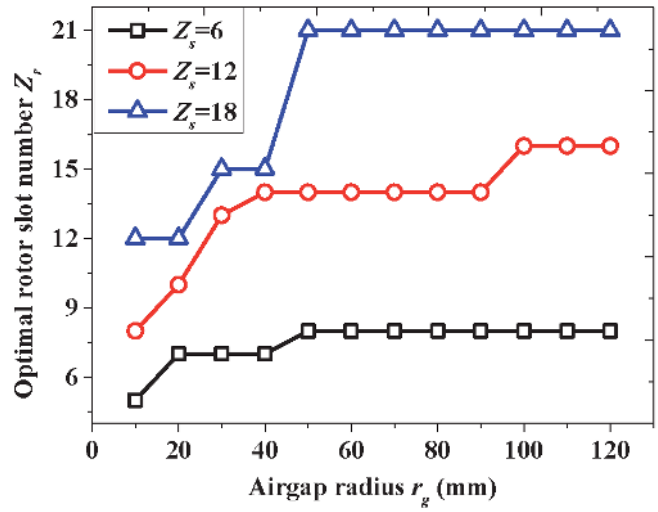

Figure 10.
Effect of r_g *on optimal* Z_r *when split ratio is 0.6.*

k_w*Z_r*B_m. Since the machine volume and PM usage are kept the same, the equivalent magnet loading B_m is mainly determined by the pole ratio (PR). So, the variation trend of torque is similar to that of k_w*Z_r*PR. It can be seen that the torque achieves the maximum value when the rotor slot number is 8, 14, and 21 for 6 stator slots, 12 stator slots, and 18 stator slots, respectively. When the recommend windings are used, which means that the winding factor are maximized, the main factor that affects the torque is the Z_r*PR. As shown in **Table 2**, the variation of PR is irregular, hence the variation of torque with rotor slot number is irregular. As can be seen, for recommended winding types, the torque achieves the maximal value when the rotor slot number is 8, 10 and 17 for 6 stator slots, 12 stator slots, and 18 stator slots, respectively.

4.1.2 Influence of airgap radius on average torque

As shown in Eq. (27), the airgap radius r_g is also very important for the output torque. **Figure 10** investigates the effect of optimal rotor slot number Z_r at different r_g. For 6, 12, 18 stator slots, their rotor slot numbers are selected as 8, 14, and 21,

respectively. Moreover, non-overlapping windings are used in these models because non-overlapping winding is simple and has the same end winding length. It can be seen that when the airgap radius is small, the optimal rotor slot number is small. This is because when the airgap radius is small, the leakage flux between adjacent rotor teeth occupies a large percent, so the optimal rotor slot number should be small to reduce the leakage flux as much as possible. When the airgap radius gets larger and larger, the leakage flux decreases gradually. Hence, the optimal rotor slot number increases.

Then, keeping the stator outer diameter as a constant, that is, 170 mm, the effects of airgap radius of average torque are analyzed in **Figure 11**. It indicates that when the airgap radius increases, the output torque goes up. This is because the torque is proportional to the square of airgap radius. The larger the airgap radius, the higher the torque. However, the torque is not only influenced by the airgap radius, but also the electric loading A_e. With the increase of airgap radius, the inner diameter of the stator increases, and thus the slot area decreases, leading to the decrease of winding turns per slot and the electric loading. Therefore, as the airgap radius keeps increasing, the output torque decreases afterwards.

4.1.3 Influence of magnetic loading and equivalent electric loading on average torque

In addition to the rotor slot number Z_r, airgap radius r_g, the rest of key parameters affecting the torque in Eq. (27) are the electric loading A_e and the equivalent magnetic loading B_m. **Figure 12** analyzes the influence of A_e and B_m on the average torque at different stator slot number. For these models, the airgap radius is fixed as 55 mm and their rotor slot number is chosen as their corresponding optimal value. Also, non-overlapping windings are adopted. As can be seen, the output torque increases with the electric loading. This reason is very simple, that is, a larger current, a higher torque. But for the equivalent magnetic loading, the variation trend of torque does not monotonically increase with the equivalent magnetic loading. This is due to the saturation effect of the iron core. Moreover, it can be seen that the knee point of the equivalent magnet loading increases with the stator slot number. Since the winding pole pair of the 18-stator-slot FRPMM is 6, which is larger than 1-winding-pole-pair of the 6-stator-slot and 4-winding-pole-pair of the

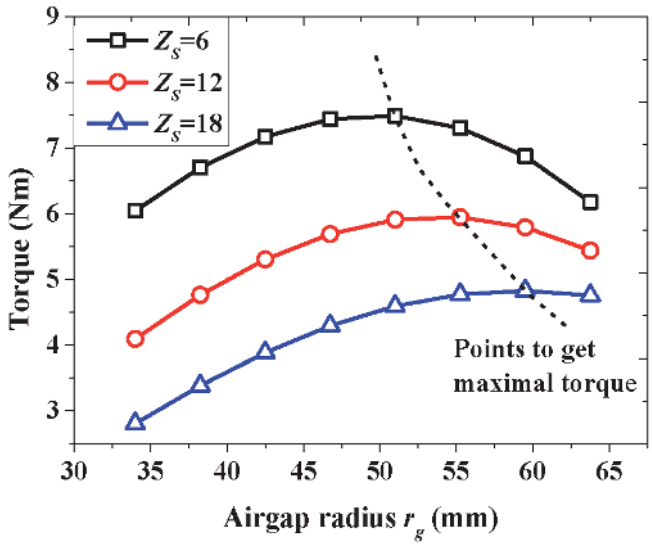

Figure 11.
Effect of r_g *on torque when stator outer diameter is 170 mm.*

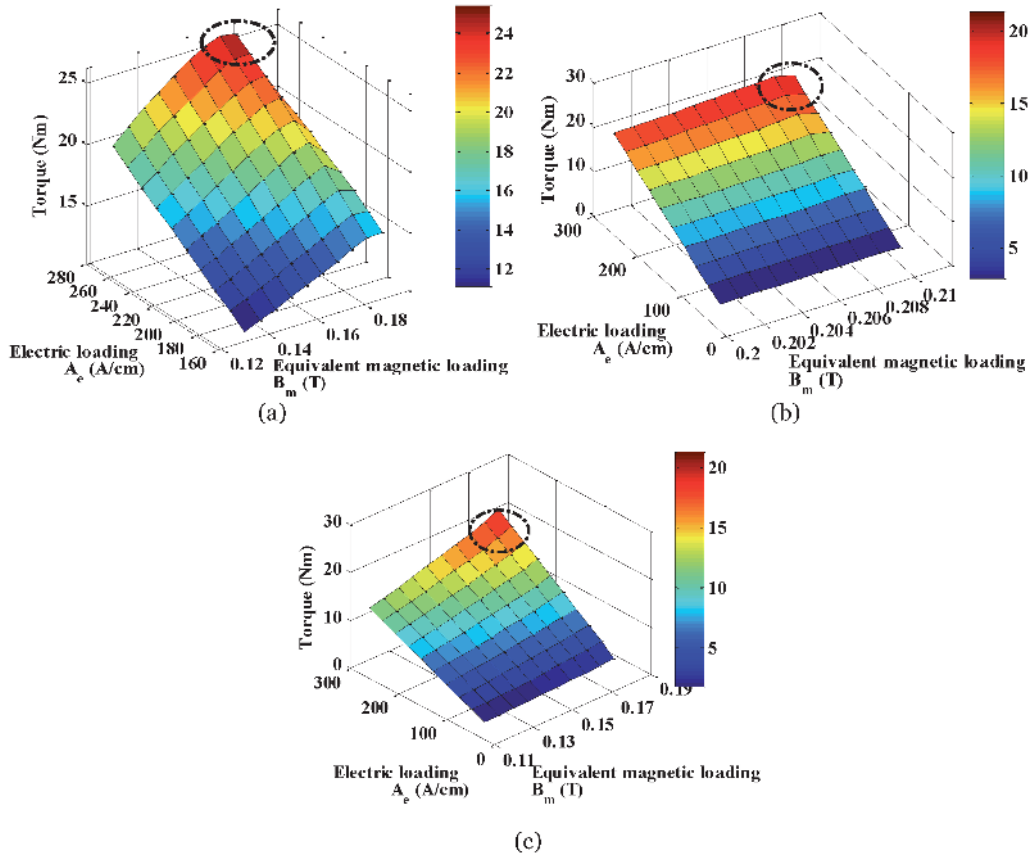

Figure 12.
Effect of equivalent magnetic loading and electric loading on torque: (a) Z_s = 6; (b) Z_s = 12; (c) Z_s = 18.

12-stator-slot FRPMM, the stator iron of the 18-stator-slot FRPMM is less likely to saturate than the others.

4.2 Pulsating torque performances

4.2.1 Influence of slot-pole combinations on pulsating torque

Apart from the torque density, pulsating torque is also very important because a large pulsating torque will increase the vibration and noise of machines. **Figure 13** shows the cogging torque and ripple torque waveforms of 13-, 14-, 16-, 17-, and 19-rotor-slot FRPMMs. The stator slot number of these models is all chosen as 12. For the rated torque, we can see in **Figure 13(b)** that the 14-rotor-slot FRPMM yields the largest among the five models. As for the pulsating torque, we can see that the cogging torque and ripple torque of 16-rotor-slot FRPMM are the largest, and that of 19-rotor-slot FRPMM is the least. This phenomenon is related to the least common multiple of stator slot number and rotor slot number. The larger least common multiple, the lower pulsating torque. The least common multiples of the 13-, 14-, 16-, 17-, and 19-rotor-slot FRPMMs are 156, 84, 48, 204, and 228, respectively. Therefore, the 19-rotor-slot FRPMM exhibit the lowest cogging torque and ripple torque. However, attentions should be paid to use odd rotor number because it will cause other problems such as eccentricity stress. **Figure 14** compares the radial stress of the five FRPMM models. It can be seen that for the even rotor slot number FRPMMs, that is, 14 and 16 rotor slots, the stress harmonics only have even orders, which will not lead to eccentricity. However, for the odd rotor slot number

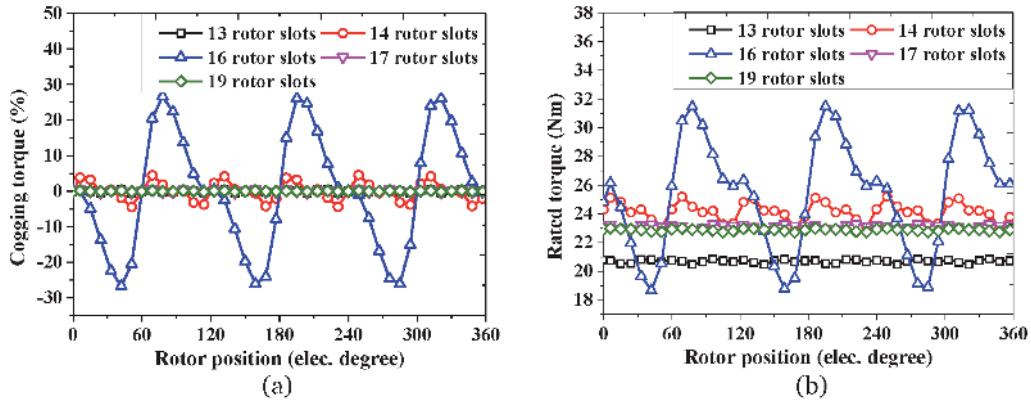

Figure 13.
Effect of slot-pole combination on pulsating torque performances: (a) cogging torque waveforms (%); (b) rated torque waveforms.

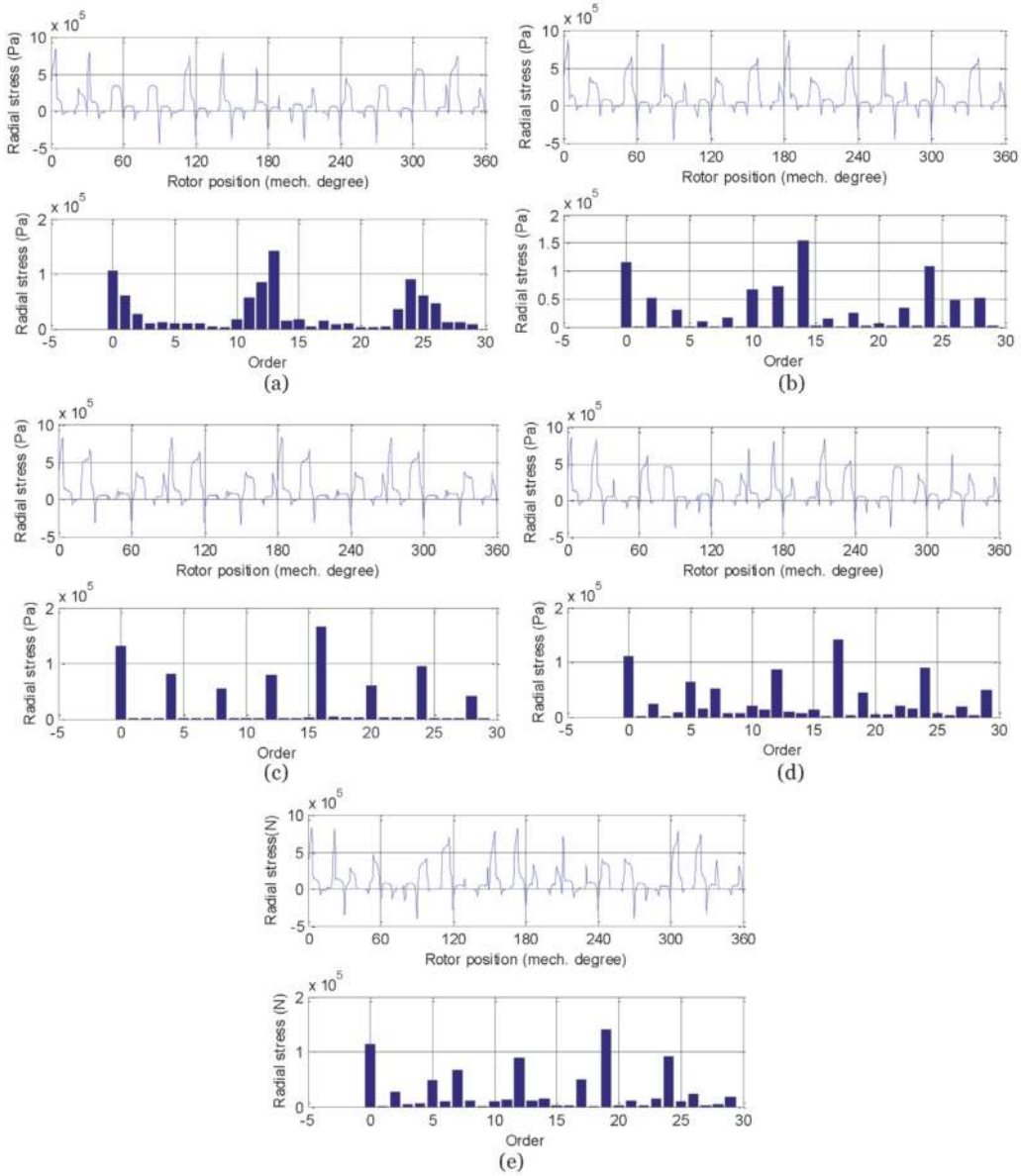

Figure 14.
Radial stress analysis of the FRPMMs: (a) 13-rotor-slot; (b) 14-rotor-slot; (c) 16-rotor-slot; (d) 17-rotor-slot; (e) 19-rotor-slot.

FRPMMs, that is, 13, 17, and 19 rotor slots, there are many odd stress harmonics. Since the first-order harmonic is dominant for the eccentricity, the 13-rotor-slot FRPMM has a large eccentricity stress. Therefore, 13-rotor-slot is not recommended. The first-order stress harmonic for 17 and 19 rotor slots are very small, so their eccentricity can be neglected.

4.2.2 Influence of PM thickness and split ratio on pulsating torque

The influences of split ratio and PM thickness on cogging torque and ripple torque of FRPMMs are also analyzed in **Figure 15**. This figure is plotted based on the 14-rotor-slot, which is chosen because it has the largest torque density and a relatively low pulsating torque, as shown in **Figure 13**. It can be found in **Figure 15(a)** that the cogging torque increases with the PM thickness and the split ratio. When the PM thickness increases, the airgap flux density increases, and thus the interaction between the PMs and slot-teeth becomes greater, which leads to a higher cogging torque. As the split ratio increases, the airgap radius increases, hence the cogging torque increases with the split ratio [30]. As for the ripple torque, the ripple torque has the maximum value when the split ratio is around 0.66. This is because the ripple torque is not only related to the slot structure but also influenced by the electric loading. As aforementioned, the pulsating torque resulting from the slot structure is increased with the split ratio. However, as the split ratio increases, the slot area is reduced and the electric loading gets smaller and smaller, so the ripple torque resulting from the electric loading becomes lower. Considering these two impacts, the ripple torque has a maximal value when the split ratio changes.

4.2.3 Influence of slot opening ratios on pulsating torque

As we know, the airgap structure is significant for the pulsating torque because the pulsating torque results from the interaction between the two sides of the airgap, that is, stator and rotor. Therefore, this chapter also analyzes the influences of stator slot opening ratio and rotor slot opening ratio on cogging torque and ripple torque. Here, the stator/rotor slot opening ratio is defined as the ratio of stator/rotor slot opening width to the stator/rotor slot pitch. **Figure 16** shows the variation of cogging torque and ripple torque with the two slot opening ratios. It can be seen that the cogging torque increases with the stator slot opening ratio. The reason is that a larger stator slot opening ratio reduces the PM width and the smoothness of PM MMF, thus the changing of the PM MMF along the tangential direction increases

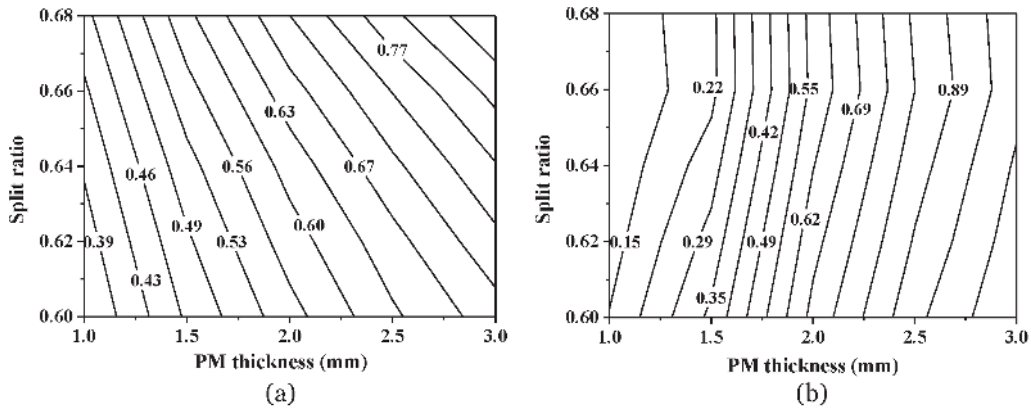

Figure 15.
Effect of split ratio and PM thickness on pulsating torque performances: (a) cogging torque (%); (b) ripple torque (%).

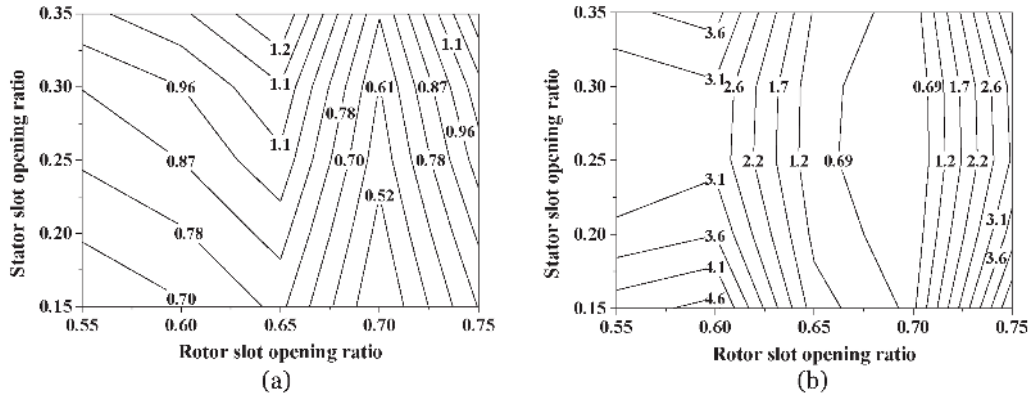

Figure 16.
Effect of stator slot opening ratio and rotor slot opening ratio on pulsating torque: (a) cogging torque (%); (b) ripple torque (%).

the cogging torque. As for the rotor slot opening ratio, which simultaneously influences all the harmonic contents of the airgap permeance, it has great and nonlinear impact on the pulsating torque. Since the pulsating torque results from the interaction of multi permeance harmonics, the variation of pulsating torque changes nonlinearly with the rotor slot opening ratio. It can be seen in **Figure 16** that the optimal cogging torque and ripple torque can be achieved when the stator slot opening ratio and rotor slot opening ratio are around 0.25 and 0.7, respectively.

4.3 Power factor performances

4.3.1 Influence of stator inner diameter and PM thickness on power factor

Since the power factor of FRPMMs is usually low, which is around 0.4–0.7, meanwhile a low power factor will increase the converter capacity and cost, the influences of key parameters on the power factor should be also analyzed to achieve a relatively high power factor. The power factor can be given as:

$$PF = 1/\sqrt{1+\left(\frac{L_s I_s}{\psi_m}\right)^2} \tag{31}$$

where I_s is the winding current, L_s is the synchronous inductance (because the saliency ratio is approximate to 1, $L_d \approx L_q$), and ψ_m is the PM flux linkage. Then, the effect of stator inner diameter on power factor is shown in **Figure 17**. Here, the stator outer diameter is kept as 124 mm, and the airgap length is fixed as 0.5 mm. It can be found that with the increase of stator inner diameter, the power factor increases continuously. The reason is that with the increase of stator inner diameter, the slot area decreases, so the winding turns per phase decreases, thus leading to the reduction of the synchronous inductance L_s. The lower L_s, the higher power factor, as shown in Eq. (31). Apart from the stator inner diameter, another important parameter affecting the power factor is the PM thickness h_m. **Figure 18** investigates the variation of power factor with respect to the PM thickness. It indicates that the power factor initially increases with the PM thickness but then decreases. The reason is explained as follows. As the PM thickness increases, the PM flux linkage ψ_m becomes larger, so the power factor increases. However, the synchronous inductance L_s also increases with the PM thickness, which leads to the reduction of power factor afterwards. Therefore, there is an optimal PM thickness for a maximum achievable power factor.

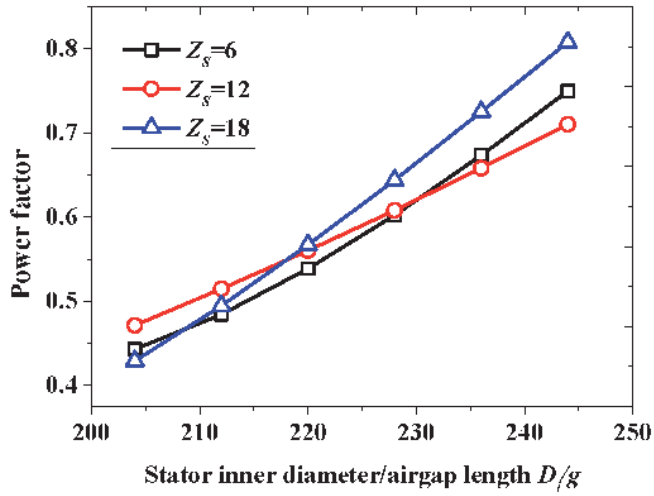

Figure 17.
Effect of stator inner diameter/airgap length on power factor.

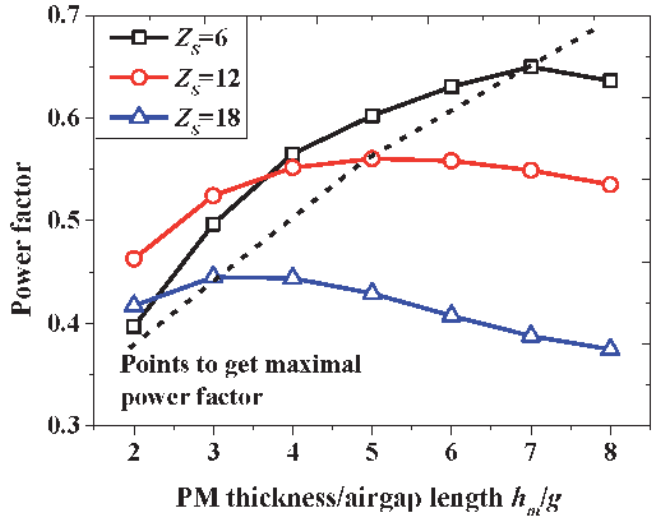

Figure 18.
Effect of PM thickness/airgap length on power factor.

4.3.2 Influence of slot opening ratio on power factor

Another important parameter that influences the airgap structure is the slot opening ratio. Hence, **Figures 19** and **20** analyzes the effect of stator slot opening ratio and rotor slot opening ratio on pulsating torque performances, respectively. It can be seen in **Figure 19** that the maximum power factor can be obtained when the stator slot opening ratio is approximately to 0.3. The explanation is as follows. When the stator slot opening ratio is too small, the slot leakage flux between the stator tips is large, thus the main flux is reduced, and the back-EMF is lowered, resulting in smaller back-EMF. And when the stator slot opening ratio is too large, the PM width will be narrower. Although the slot leakage flux is reduced, the main flux is not high due to the narrower PMs, thus the back-EMF is lowered. Therefore, the stator slot opening ratio cannot be too small or too large, that is, there is an optimal value for the stator slot opening ratio.

Then, the influences of rotor slot opening ratio on power factor can be seen in **Figure 20**. It indicates that when the rotor slot opening ratio is around 0.7, the

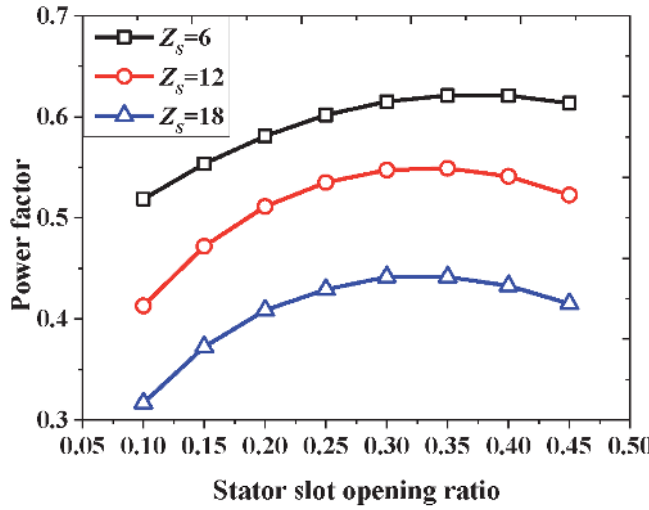

Figure 19.
Effect of stator slot opening ratio on power factor.

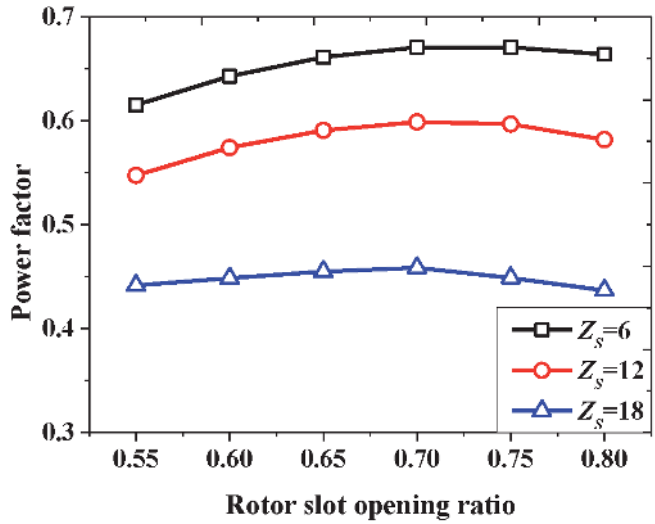

Figure 20.
Effect of rotor slot opening ratio on power factor.

power factor reaches the maximal value. This is because the power factor is mainly influenced by the back-EMF. When the rotor slot opening ratio increases, the effective airgap length becomes smaller, thus the main flux is increased and the back-EMF is improved. As a result, the power factor is increased. When the rotor slot opening ratio keeps increasing, the flux modulation effect of the rotor teeth becomes weaker and weaker, thus the smaller modulated flux, and the lower back-EMF. Therefore, there is also an optimal value for rotor slot opening ratio when a high power factor is demanded.

4.4 PM demagnetization performances

For PM machines, PM demagnetization performances are very important because it is highly related to the safe operation and machine reliability. Therefore, the PM demagnetization performances of FRPMMs should be analyzed in this

chapter. Since the magnetic properties of PM materials are sensitive to temperature, and the temperature coefficient of NdFeB magnet is as high as $-0.126\%K^{-1}$. When the current of FRPMMs is large, the winding heating can easily affect the PMs attached to the stator teeth surface, causing the decrease of PM magnetic performances. On the other hand, when the winding current is large, the demagnetizing effect of the armature field is enhanced, and thus the PMs have the possibility to be demagnetized. Therefore, it is of great importance to investigate the PM demagnetization performances of FRPMMs at different conditions.

Figure 21 shows the demagnetization curve of the magnets. The upper half is a straight line, and lower half under the knee point B_{knee} is a curved line. When the FRPMM works on the straight line (such as point P_1), the return line coincides with the demagnetization curve, and the magnetic performance of the magnets will not be lost. However, when the armature equivalent MMF H_a' is too large at load condition, or the knee point is too high, the working point B_{knee} is moved to P_2. At this time, the recovery line does not coincide with the original demagnetization line, thus the intersection of the B-axis changes from B_r to B_{r1}, causing the irreversible demagnetization. Then, the PM properties and machine performances will no longer return to the original. So, the PM flux density should be examined in order to check the risk of irreversible demagnetization. As we know, the PM flux density is determined by the design parameters such as electric loading A_e, PM thickness h_m, rotor slot opening ratio, etc. So, in this chapter, the effects of electric loading A_e, PM thickness h_m, rotor slot opening ratio b_o/t on PM demagnetization performances of FRPMMs will be studied. For instance, the PM material is selected as N38SH, and knee point of the PM flux density at 100°C is 0.35 T.

Figure 22 shows the PM flux density of a 12-stator-slot/14-rotor-slot FRPMM when the electric loading A_e is 1600A/cm, the PM thickness h_m is 3 mm, rotor slot opening ratio b_o/t is 0.65. It can be seen that the PM flux density distribution varies with the rotor position. When the rotor position is 140°, the PM does not demagnetize, while at 0° and 340°, the PM will demagnetize. Hence, in the following analysis, the PM flux density at the most severe moment of demagnetization is selected.

Figure 23 studies the magnetic flux density distribution in the PMs under different electric loadings. It can be found that the larger electric loading A_e, the smaller minimum flux density. This is because the larger electric loading, the higher armature MMF H_a', and the more left operating point P_2, so the lower flux density

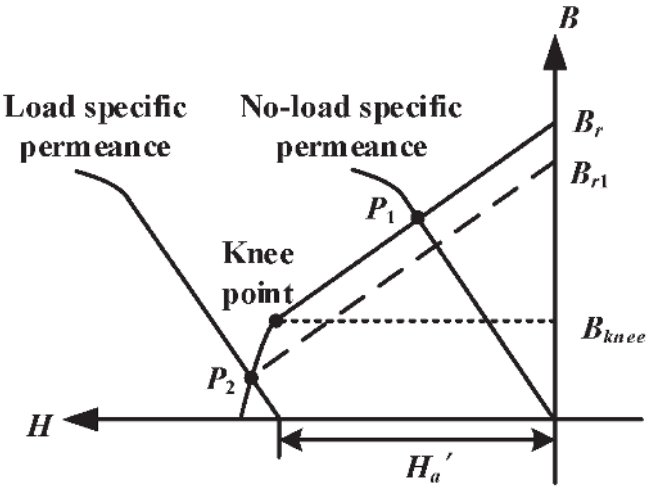

Figure 21.
PM demagnetization curve.

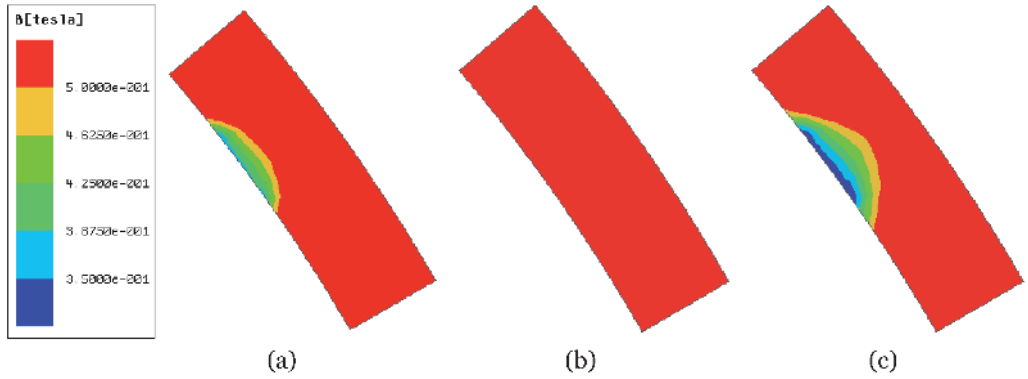

Figure 22.
PM demagnetization at different rotor positions: (a) rotor position = 0°; (b) rotor position = 140°; (c) rotor position = 340°.

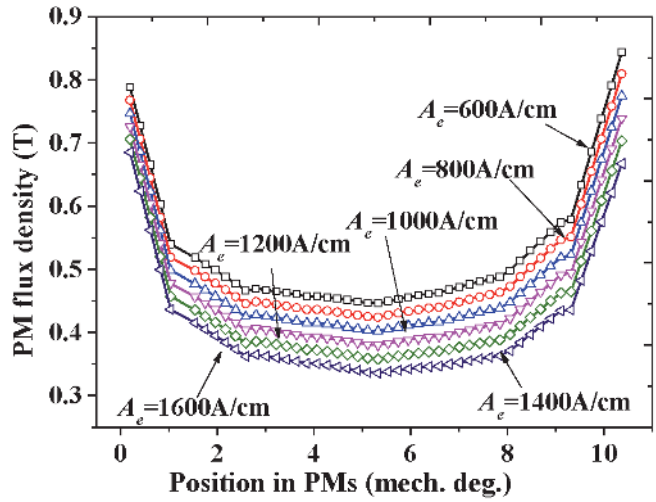

Figure 23.
Influence of A_e *on PM demagnetization.*

in the magnets. When the electric loading A_e is 1400A/cm, the PM irreversible demagnetization just occurs. In addition, it can be seen that the entire magnetic flux density map is skewed to the right. This is because the N-pole magnet is intercepted in this analysis, and there is an S-pole magnet next to the N-pole magnet. There is PM pole leakage flux between the S-pole magnet (negative axis) and the N-pole magnet (positive axis), so the magnetic flux density around the 0 position is lower, and away from the 0 position, the magnetic flux density gradually rises.

Figure 24 analyzes the effect of PM thickness h_m on the PM demagnetization performances. At this time, the electric loading is chosen as 800 A/cm, and the rotor slot opening ratio is selected as 0.65. It can be seen in **Figure 24** that when the PM thickness h_m is less than 2.5 mm, the irreversible demagnetization will happen, while when the PM thickness h_m is larger than 2.5 mm, the irreversible demagnetization will not. In this model, the airgap length is 0.5 mm. Therefore, in the design stage, the PM thickness should be better to set as five times or more the airgap length. Considering the back-EMF, it is claimed in [3] that when the PM thickness is about three times the airgap length, the back-EMF will reach the maximum. But considering both back-EMF and PM demagnetization risk, it is safer to set the PM thickness as about five times airgap length.

Figure 25 shows the influences of rotor slot opening ratio b_o/t on the flux density distribution inside the PMs. At this time, the electric loading is chosen as 800 A/cm,

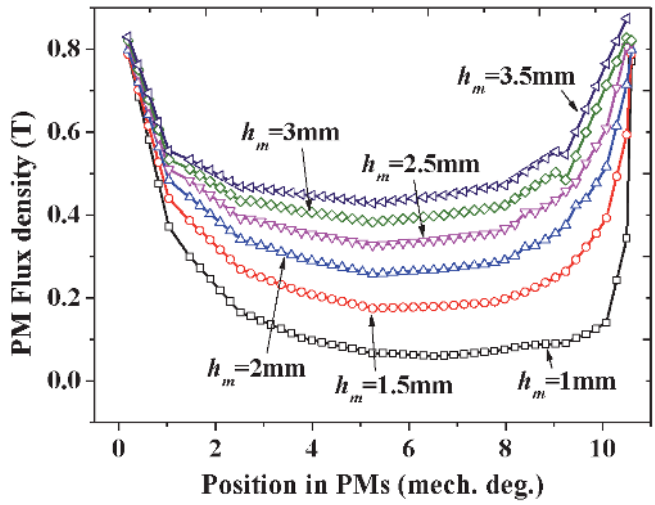

Figure 24.
Influence of h_m *on PM demagnetization.*

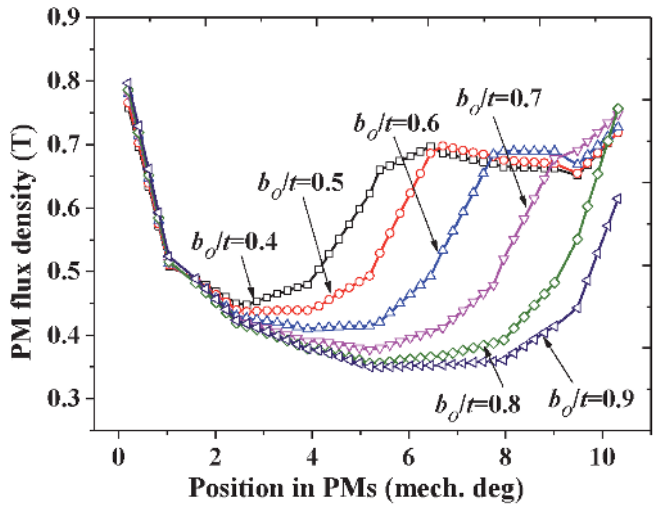

Figure 25.
Influence of b_o/t *on PM demagnetization.*

and the PM thickness is selected as five times the airgap length, that is, 3 mm. The larger rotor slot opening ratio, the narrower rotor teeth, thus the more saturated rotor teeth, and the smaller magnetic reluctance. As shown in **Figure 20**, when the magnetic gets smaller, the more left operating point P_2, and thus the lower PM flux density. It can be seen in **Figure 25** that when the rotor slot opening ratio b_o/t is 0.9, the irreversible PM demagnetization just occurs. In Ref. [28], it is claimed that the maximum back-EMF can be achieved when the rotor slot opening ratio b_o/t is around 0.6. So, during the design process, the optimal rotor slot opening ratio can be directly applied without consideration of the PM demagnetization risk.

5. Geometric design of stator and rotor

5.1 Stator design

The geometrical parameters of stator and rotor are shown in **Figure 26**. The no-load flux of each winding pole could be calculated as:

$$\phi_m = 2\lambda_w l_{stk} B_m / \pi \tag{32}$$

where λ_w is the winding pitch. If full-pitch winding is adopted, the winding pitch is able to be written as:

$$\lambda_w = 2\pi r_g / 2P \tag{33}$$

Then, the no-load flux of each winding pole ϕ_m in Eq. (32) could change to:

$$\phi_m = 2 r_g l_{stk} B_m / P \tag{34}$$

Defining the average flux density at the stator yoke as B_y, the stator yoke thickness h_y can therefore be deduced as:

$$h_y = \frac{\phi_m}{2 B_y k_{stk} l_{stk}} = \frac{r_g B_m}{P B_y k_{stk}} \tag{35}$$

Similarly, defining the average flux density at the middle of stator tooth as B_t, the stator tooth width is able to be worked out:

$$w_t = \frac{\phi_m}{3SPP k_{stk} l_{stk} B_t} = \frac{4 r_g B_m}{Z_s k_{stk} B_t} \tag{36}$$

Moreover, in order to simultaneously maintain a relatively large torque density as well as reduce the risk of PM demagnetization, the PM thickness is recommended to be:

$$h_m = 4g \sim 6g \tag{37}$$

where g is the airgap length. Since the optimal torque density is often obtained when the slot opening ratio is approximate to 0.25 [28], the stator slot opening width w_o could be written as:

$$w_o = \pi \left(r_g + h_m \right) / 2 Z_s \tag{38}$$

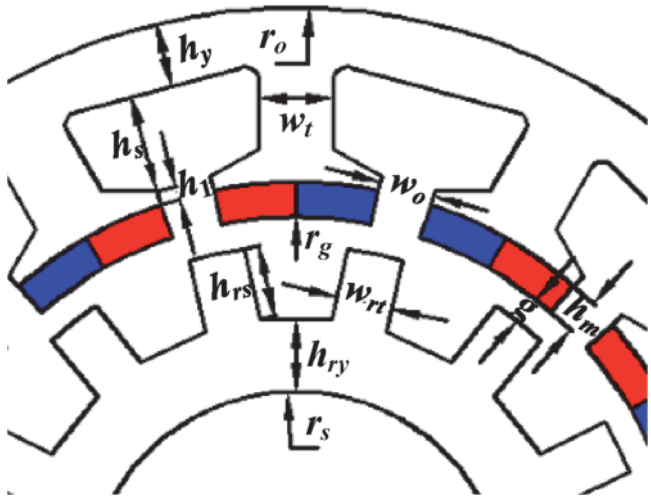

Figure 26.
Geometry of stator and rotor.

Then, next step is to calculate the stator outer radius r_o. Firstly, the total slot area of all the stator slots A_{slot} can be written based on the winding electric loading A_e and the current density J_e:

$$A_{slot} = 2\pi(r_g + h_m)A_e/J_e S_{fg} \tag{39}$$

where S_{fg} is the slot fill factor. Meanwhile, the total slot area of all the stator slots A_{slot} can be also derived out using the structural parameters:

$$A_{slot} = \pi(r_g + h_m + h_1 + h_s)^2 - \pi(r_g + h_m + h_1)^2 - Z_s w_t h_s \tag{40}$$

Combining the Eqs. (39) and (40), the slot depth h_s can be determined. Then, the stator outer radius r_o can be given as:

$$r_o = r_g + h_m + h_1 + h_s + h_y \tag{41}$$

5.2 Rotor design

Defining the average flux density of each rotor yoke and middle of rotor tooth as B_{ry}, and B_{rt}, respectively, the rotor yoke thickness h_{ry} and rotor tooth width w_{rt} are able to be achieved using the similar derivation procedure as Eq. (35) and Eq. (36). Finally, the h_{ry} and w_{rt} are given as:

$$h_{ry} = r_g B_m / Z_r B_{ry} k_{stk} \tag{42}$$

$$w_{rt} = 4 r_g B_m / Z_r k_{stk} B_{rt} \tag{43}$$

Then, the rotor slot depth h_{rs} is determined as:

$$h_{rs} = r_s + h_{ry} \tag{44}$$

6. Design methodology and evaluations

6.1 Design procedure

Based on the analytical equations and the investigations of key performances in the former parts, a quick and accurate analytical design of a FRPMM can be realized by following these procedures (as depicted in **Figure 27**):

1. Based on the performance investigations in **Figures 9–24**, the initial design values, including combination of stator slot and rotor slot number, electric loading, equivalent magnetic loading, airgap length, materials of active parts, etc. can be firstly selected.

2. Then, assuming an appropriate aspect ratio k_{lr}, the airgap radius r_g, and the stack length l_{stk} can be worked out using Eqs. (29) and (30).

3. Based on Eqs. (32–44), the detailed geometric parameters of the stator core and the rotor core are able to be obtained. Therefore, the stator outer diameter r_o and machine total length l_o can be finally determined.

4. After that, check if the stator outer diameter and the machine total length satisfy the required design specifications. If so, proceed to the FEA

verifications of machine performances. If not, reset the initial values such as combination of stator slot and rotor slot number, electric loading, equivalent magnetic loading, etc.

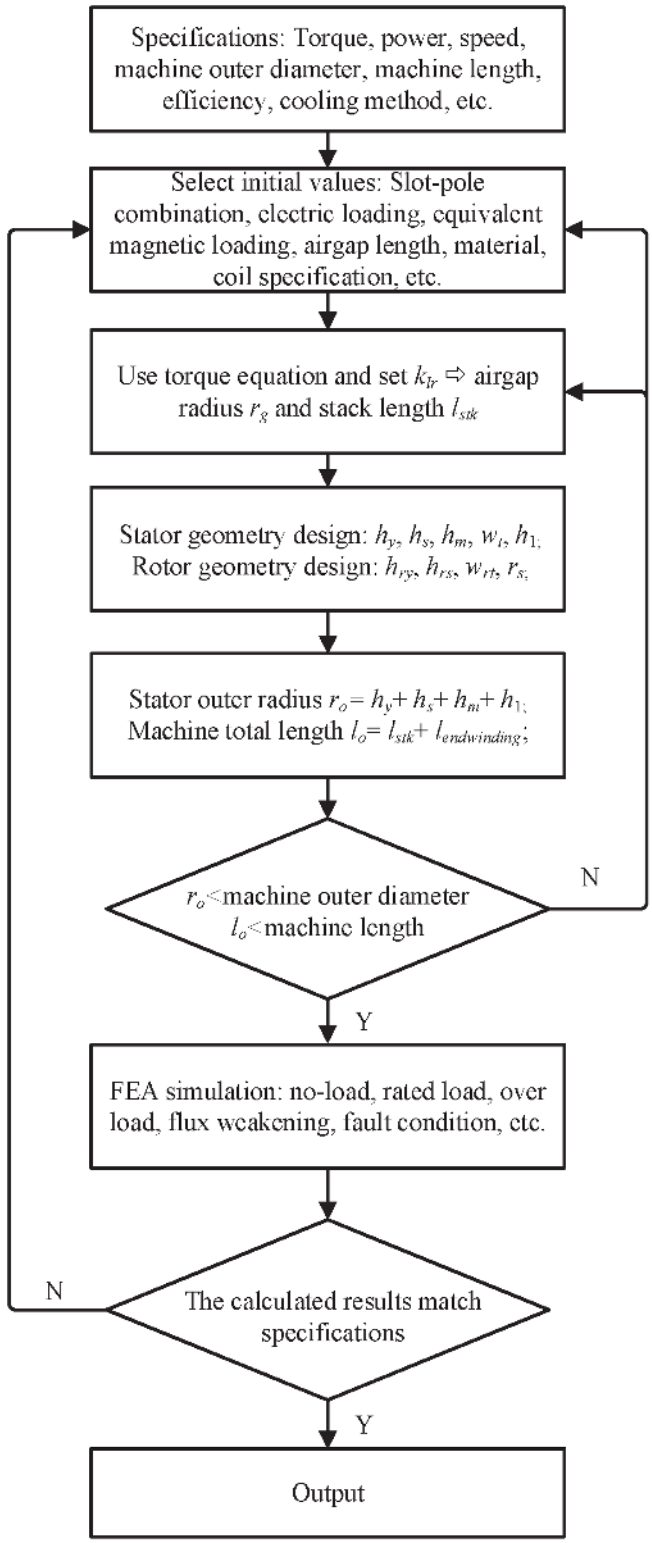

Figure 27.
Design flow of FRPMM.

5. Conducting FEA simulations, the electromagnetic performances such as back-EMF, average torque, pulsating torque, power factor, efficiency, etc. can be obtained. Check if all the performances satisfy the design specifications. If not, adjust the design parameters in the former steps and iterate the design flow until every output meets the requirement.

6. Finally, it is the result output.

6.2 Case study

In order show the effectiveness of the introduced analytical method, a FRPMM is designed based on the method. **Table 4** shows the specifications of the FRPMM, which mainly includes the rated torque, machine volume, cooling method, rated power, and speed. According to the rated torque, a design margin of 5% is suggested so as to make sure the torque output. Therefore, the requirement of the torque is 8.4 Nm for this design. Then, the combination of stator slots and rotor slots is determined in the first place. This combination is selected due to its high torque density and low pulsating torque, as shown in **Figure 13**. Then, since the cooling method is natural cooling, the electric loading and the equivalent magnetic loading are chosen as 300A/cm and 0.2 T, respectively. After that, based on the output torque value 8.4 Nm and Eq. (29), the airgap radius is determined as 38.5 mm. Furthermore, assuming the yoke flux density of stator core and rotor core as 1.0 T, and the teeth flux density of stator core and rotor core as 1.2 T, the detailed

Parameter	Value	Parameter	Value
Rated torque	8 Nm	Rated speed	300 rpm
Rotor inner diameter	32 mm	PM material	N38SH
Stator outer diameter	130 mm	Stack length	120 mm
Airgap length	0.6 mm	Iron material	50WW470
Cooling method	Natural cooling	Rated power	0.25 kW

Table 4.
Design specifications of a three-phase FRPMM.

	Parameter	Value	Parameter	Value
Stator	Outer diameter	124 mm	Inner diameter	79 mm
	Turns per phase	300	Teeth width	11.5 mm
	Slot number	12	Yoke thickness	6 mm
	Slot depth	13.5 mm	Yoke flux density	1.0 T
	Winding pole pair	1	Teeth flux density	1.1 T
Magnet	PM thickness	3 mm	Magnet width	7.8 mm
Rotor	Outer diameter	77.8 mm	Slot depth	10.4 mm
	Teeth flux density	1.2 T	Yoke thickness	12.5 mm
	Inner diameter	32 mm	Yoke flux density	1.0 T
	Teeth width	4 mm	Slot number	17

Table 5.
Design parameters of the FRPMM using the design method.

Parameter	Analytical design method	FEA
PM flux linkage	1.43 Wb	1.35 Wb
Back-EMF	44.8 V	42.4 V
Torque	8.4 Nm	7.97 Nm

Table 6.
Results comparison of the design method and 2D FEA.

Figure 28.
12-slot/17-pole FRPMM prototype: (a) stator; (b) rotor.

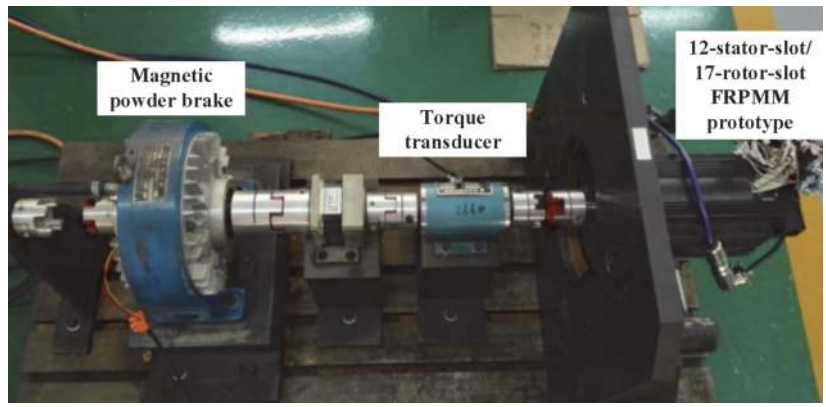

Figure 29.
Test bed of the FRPMM prototype.

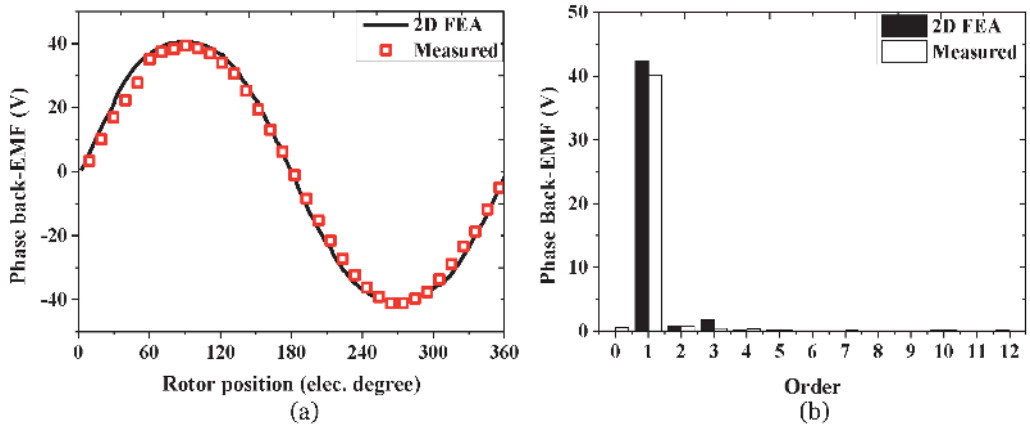

Figure 30.
Back-EMF waveforms at rated speed 300 rpm: (a) waveform; (b) FFT analysis.

DOI: http://dx.doi.org/10.5772/intechopen.92428

geometric parameters can all be determined. At last, the stator outer diameter is worked out as 124 mm, which is less than the requirement 130 mm. So far, this design is effective. **Table 5** summarizes the design parameters of the FRPMM. Finally, in order to verify the accuracy of the proposed analytical design method, the FEA model is built, and the simulated performances are compared to the analytical designed values. It can be seen in **Table 6** that the FEA simulated results match well with the analytical method. More importantly, the simulated performance output satisfies the design specifications. Therefore, this analytical design is successful.

6.3 Experimental study

To verify the calculated results by the analytical method and FEA, the FRPMM prototype has been built. Its major parameters are listed in **Table 4**. The structure and test bed of the prototype are shown in **Figures 28** and **29**, respectively.

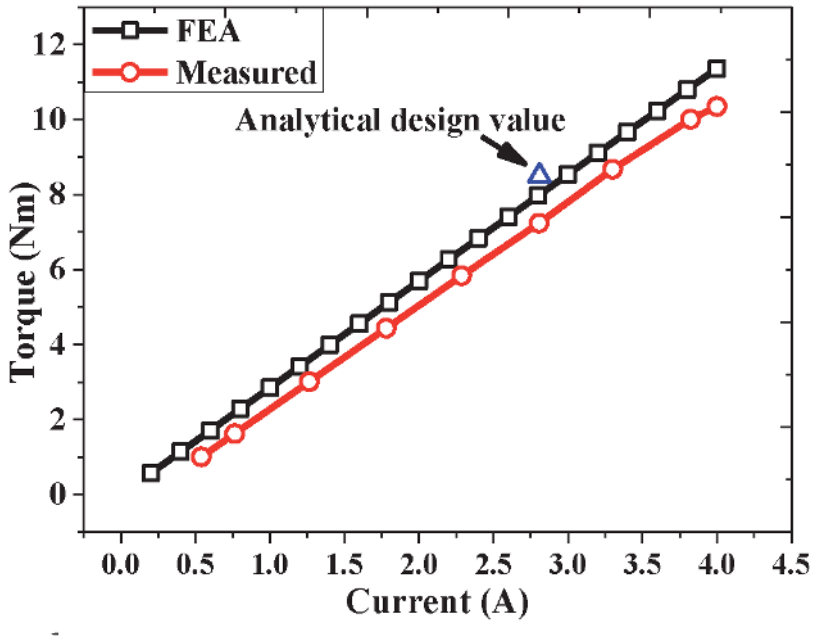

Figure 31.
Output torque vs. phase current.

Parameter	FEA	Experiment
Average torque at rated current	7.97 Nm	7.24 Nm
Torque per weight	0.66 Nm/kg	0.60 Nm/kg
Phase back-EMF magnitude at 300 rpm	42.4 V	41.2 V
THD of the phase back-EMF at 300 rpm	1.26%	2.63%
Total losses	99.5 W	116.7 W
Efficiency	60.3%	57.3%
Power factor	0.756	0.746

Table 7.
Result comparison of FEA and experiment of the FRPMM prototype.

Figure 30 compares the phase back-EMF waveform and spectrum at 300 rpm. It can be seen that the back-EMF waveforms are very sinusoidal. This is because the total harmonic distortion (THD) of FEA and experiments are only 1.26% and 2.63%, respectively. The sinusoidal back-EMF is inherent without any special design techniques such as skewing or pole shaping. Then, **Figure 31** shows the FEA simulated and experimental results of average torque at different winding current values. In addition, the analytical design value is also plotted as the blue triangle. It indicates that the simulated, analytical and experimental results have reached good agreements. Finally, **Table 7** compares the electromagnetic performances by FEA and experiments. Thus, the feasibility of the analytical design method can be seen.

7. Conclusions

The design of FRPMMs is usually based on time-stepping FEA, which are accurate but time-consuming. To save the design time meanwhile maintain the accuracy, this chapter proposes an analytical design method of FRPMMs. First, the sizing equation is derived, and then the dimensional parameters of stator and rotor are calculated. Finally, based on the above equations, an analytical design procedure is established. Moreover, in order to help to choose the initial design parameters in the sizing equation, including number of stator slots and rotor slots, airgap radius, electrical loading, and equivalent magnetic loading, their effects on the average torque, cogging torque, torque ripple, and power factor are investigated, providing reliable guidance for designers. At last, in order to make the introduced design methodology easier to understand, a FRPMM is designed and tested.

Acknowledgements

This work was supported by National Natural Science Foundation of China (NSFC) under Project Number 51807076, and Alexander von Humboldt Foundation.

Nomenclature

B_r	remanent flux density
μ_r	relative permeability of magnets
g'	effective airgap length considering PM thickness
h_m	PM height along the magnetization direction
SO	stator slot opening ratio (=slot opening width/slot pitch)
g	airgap length
r_g	airgap radius
N_s	number of series turns per phase
P	number of stator winding pole pairs
l_{stk}	active stack length
Z_r	number of rotor teeth
ω_m	mechanical angular speed of rotor
Z_s	number of stator teeth
SPP	slot per pole per phase
θ	angular position of rotor axis with respect to the axis of phase a
θ_s	particular position in the stator reference frame measured from the axis of phase a
PR	pole ratio (=rotor pole number/winding pole pair)

DOI: http://dx.doi.org/10.5772/intechopen.92428

Author details

Yuting Gao[1*] and Yang Liu[2]

1 Karlsruhe Institute of Technology, Karlsruhe, Germany

2 Wuhan Institute of Marine Electric Propulsion, Wuhan, China

*Address all correspondence to: gyt626890@gmail.com

References

[1] Upadhyay P, Sheth NK, Rajagopal KP. Effect of rotor pole arc variation on the performane of flux reversal motor. In: International Conference on Electrical Machines and Systems. 2007. pp. 906-911

[2] Sheth NK, Rajagopal KR. Performance of flux reversal motor at various rotor pole arcs. In: International Conference on Electrical Machines and Systems. 2007. pp. 1517-1522

[3] Kushwaha D, Dwivedi A, Reddy R, et al. Study of 8/12 flux reversal machine as an alternator. In: Eighteenth National Power Systems Conference. 2014. pp. 1-4

[4] Shin HK, Kim TH, Kim CJ. Demagnetization characteristic analysis of inset-type flux-reversal machines. In: 15th International Conference on Electrical Machines and Systems. 2012. pp. 1-4

[5] Vandana R, Fernandes BG. Mitigation of voltage regulation problem in flux reversal machine. In: Energy Conversion Congress and Exposition. 2011. pp. 1549-1554

[6] More DS, Fernandes BG. Novel three phase flux reversal machine with full pitch winding. In: International Conference on Power Electronics. 2007. pp. 1007-1012

[7] Ahn J, Choi JH, Kim S, et al. Parametric variance consideration in speed control of single-phase flux reversal machine. IET Electric Power Applications. 2008;**2**(4):266-274

[8] Kim TH, Won SH, Lee J. Finite element analysis of flux-reversal machine considering BEMF current of a switch-off phase and v-i characteristics of a transistor and a freewheeling diode. IEEE Transactions on Magnetics. 2006; **42**(4):1039-1042

[9] Wang C, Nasar SA, Boldea I. High speed control scheme of flux reversal machine. In: International Conference on Electric Machines and Drives. 1999. pp. 779-781

[10] Deodhar R, Andersson S, Boldea I, Miller T. The flux-reversal machine: A new brushless doubly-salient permanent-magnet machine. IEEE Transactions on Industry Applications. 1997;**33**(4):925-934

[11] Wang CX, Boldea I, Nasar SA. Characterization of three phase flux reversal machine as an automotive generator. IEEE Transactions on Energy Conversion. 2001;**16**(1):74-80

[12] Lee CHT, Chau KT, Liu C, et al. A new magnetless flux-reversal HTS machine for direct-drive application. IEEE Transactions on Applied Superconductivity. 2015;**25**(3):5203105

[13] Prakht V, Dmitrievskii V, Klimarev V, et al. High speed flux reversal motor for power tool. In: International Electric Drives Production Conference. 2016. pp. 306-311

[14] Bahrami H, Zabihi A, Joorabian M. A novel flux-reversal axial flux generator for high speed applications. International Conference on Power Electronics and Drives Systems. 2005;**2**: 1152-1155

[15] Prakht V, Prakht V, Sarapulov S, et al. A multipole single-phase SMC flux reversal motor for fans. In: International Conference on Electrical Machines. 2016. pp. 53-59

[16] Dmitrievskii V, Prakht V, Mikhalitsyn A. A new single-phase flux reversal motor with the cores made of

soft magnetic composite materials. In: International Conference on Electrical Machines and Systems. 2015. pp. 936-939

[17] Pellegrino G, Gerada C. Modeling of flux reversal machines for direct drive applications. In: European Conference on Power Electronics and Applications. 2011. pp. 1-10

[18] More DS, Kalluru H, Fernandes BG. Outer rotor flux reversal machine for rooftop wind generator. In: International Conference on IEEE Industry Application Society Annual Meeting. 2008. pp. 1-6

[19] Lee CHT, Chau KT, Liu C. Design and analysis of a cost-effective magnetless multiphase flux-reversal DC-field machine for wind power generation. IEEE Transactions on Energy Conversion. 2015;**30**(4): 1565-1573

[20] Li T, Sun Y, Li G, et al. Design of a novel double salient permanent magnet machine for wind power generation. In: International Conference on Electrical Machines and Systems. 2010. pp. 1053-1056

[21] Boldea I, Zhang L, Nasar SA. Theoretical characterization of flux reversal machine in low-speed servo drives-the pole-PM configuration. IEEE Transactions on Industry Applications. 2002;**38**(6):1549-1557

[22] Li W, Chau KT, Ching TW. A six-phase transverse-flux-reversal linear machine for low-speed reciprocating power generation. In: IEEE International Electric Machines and Drives Conference. 2015. pp. 618-623

[23] Gandhi A, Mohammadpour A, Sadeghi S. Doubled-sided FRLSM for long-stroke safety-critical applications. In: IEEE Industrial Electronics Society Annual Conference. 2011. pp. 4186-4191

[24] Chung S, Lee H, Sang M. A novel design of linear synchronous motor using FRM topology. IEEE Transactions on Magnetics. 2008;**44**(6):1514-1517

[25] Boldea I, Wang CX, Nasar SA. Design of a three-phase flux reversal machine. Electric Machines and Power Systems. 1999;**27**:849-863

[26] Kim TH, Lee J. A study of the design for the flux reversal machine. IEEE Transactions on Magnetics. July 2004; **40**(4):2053-2055

[27] Kim B, Lipo TA. Operation and design principles of a PM Vernier motor. IEEE Transactions on Industry Applications. March 2014;**50**(6): 3656-3663

[28] Gao Y, Qu R, Li D, et al. Design procedure of flux reversal permanent magnet machines. IEEE Transactions on Industry Applications. 2017;**53**(5): 4232-4241

[29] Zhu ZQ, Howe D. Instantaneous magnetic-field distribution in brushless permanent-magnet dc motors, Part III. Effect of stator slotting. IEEE Transactions on Magnetics. 1993;**29**(1): 143-151

[30] Gao Y, Qu R, Li D, et al. Torque performance analysis of three-phase flux reversal machines for electric vehicle propulsion. IEEE Transactions on Industry Applications. 2017;**53**(3): 2110-2119